Selective Laser Melting Finite Element Modeling: Validation with High-Speed Imaging and Lack of Fusion Defects Prediction

C. Bruna-Rosso[a,*], A.G. Demir[a], B. Previtali[a]

[a]*Dipartimento di Meccanica, Politecnico di Milano, Via la Masa 1, Milan, Italy*

Abstract

Selective laser melting (SLM) is a fast-growing technology which still lacks knowledge and management for wider industrial use. Numerical modeling is today a standard tool in the manufacturing industry to support design and process parameters determination. It is thus of great importance to experimentally validate the simulations in order to ensure their predictive capabilities. However, the fast nature of the process complicates observation of the quantities required for the simulation validation. A finite element model (FEM) of the SLM process is proposed here, together with its numerical validation by comparison with the literature, and experimental validation using high-speed imaging. The melt pool widths and lengths retrieved from the simulation and the videos were measured. The model demonstrated a good accordance with both the literature and the experimental results. Reduced melt pool geometries were simulated in the first tracks which led to lack of fusion defect formations.

Keywords: Selective Laser Melting, Finite Element Modeling, High-Speed Imaging

Highlights

- SLM process simulation development, calibration, and validation are presented.
- A thermal FE model was implemented to predict phase transformations.
- A heat source was calibrated using high-speed imaging and metallographic analysis.
- Process validation was carried out using real time high-speed images of the melt pool.
- Simulations of multiple track scans were used to analyze lack-of-fusion formation.

*Corresponding author

Email addresses: claire.brunarosso@polimi.it (C. Bruna-Rosso), aligokhan.demir@polimi.it (A.G. Demir), barbara.previtali@polimi.it (B. Previtali)

Graphical Abstract

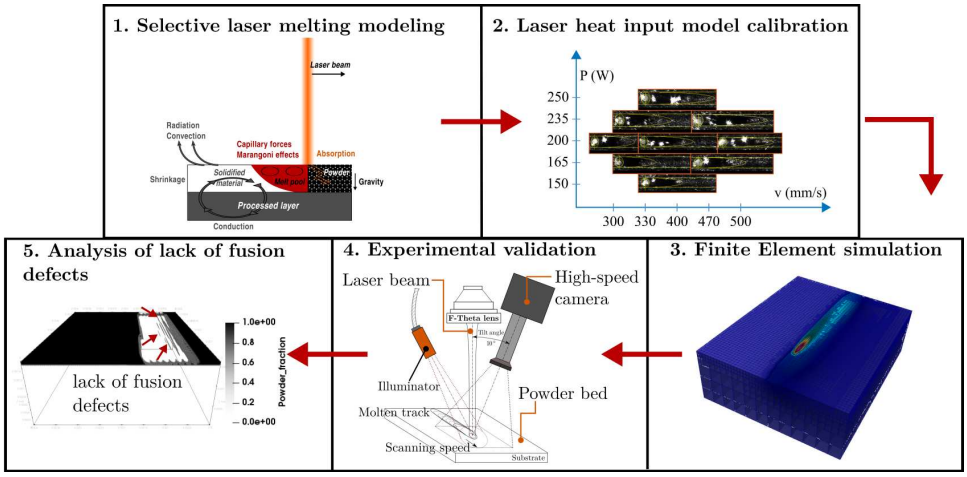

1. Introduction

Selective laser melting (SLM) is one of the layer-based additive manufacturing processes. Using this technique, functional parts can be built layer by layer to obtain a final 3D geometry that could not be reached by traditional manufacturing processes. Moreover, the highly concentrated heat input provided by the laser enlarges the range of processable materials to include metal [1]. The extended variety of manufacturable geometry and materials make this technology particularly suitable for fields such as the biomedical industry and aeronautics [2]. However, the process still relies on trial-and-error learning and SLM produced parts are still quite often not qualified, which limits the industrial development of this technology [3]. A first way to gather knowledge about a process is to use empirical methods such as design of experiment [4]. However, experimental characterization of a process may become time and resource consuming, and empirical modeling is often restrained to the application it was developed for and is hardly expandable [5]. In a common approach, simple geometries are produced with variable process parameters and part density is measured. Such an approach is effective, though is limited to being extended to smaller features or bulky components. Moreover, other defects such as thermal distortions require an estimation of the thermal gradients generated during the process. Gaining a better insight of the process through a reliable and realistic physical model can offer a good alternative [6]. One key challenge is then to ensure that the model generates sufficiently accurate results in a limited amount of time, not exceeding the experimentation cost. Despite various attempts to simulate the process (as reviewed by [7], or more recently [8, 9, 10] for example), experimental validation of SLM models is indeed still an open issue that has been sparingly discussed in the recent literature. Many models have been validated employing post-experiment melt pool measurement by observing the metallographic cross-sections of the produced samples [11, 12, 13]. The major advantage of this technique is its practical simplicity and availability. It has however two major drawbacks: first it is not an on-line measurement, and second it is destructive. To address those issues Denlinger et al. [14] developed

a thermocouple setup. Nevertheless, due to the limitations in terms of maximal measurable temperature and response time of said device, the measurements are performed away from the molten pool which is the most critical area. Cheng et al. [15] developed a setup for electron beam melting using a near infrared thermal camera. The major advantage of this method is the possibility to register on-line melt pool temperatures. However, the reliability of the measurements is strongly related to a complex calibration procedure and the temporal resolution of said device (60Hz) is limited which does not allow all the melt pool dynamics, which contain very fast phenomena, to be caught. High-speed imaging (HSI) can address this issue since it allows to take up to hundreds of thousands of images per second. Previous use of this technology for model validation purposes is reported in [16] and [17]. Riedlbauer et al. used HSI to monitor the presence of molten material but no quantitative measurements of the melt pool were taken on the recorded images. On the second article, Scipioni et al. used the high-speed videos, recorded with a camera mounted coaxially with the laser beam, to estimate the cooling rates and measure the melt pool length on a reduced area of single-track experiments. Evidently, literature lacks a direct on-line comparison between observed and simulated melt pool geometries. A finite element model (FEM) is proposed here, together with its numerical validation against the literature [18, 19] and its experimental validation using HSI. A full single-layer multi-track experiment was recorded with a fixed high-speed camera and the corresponding simulation was run for comparison. To the authors knowledge, no previous work has attempted to provide a full framework of process modeling that involves all steps from model development, to its experimental calibration and its validation with in-situ melt pool geometry measurements.

The paper presents a complete strategy dedicated to the development of an SLM finite element model. First, an in-house thermal FEM able to compute the melt pool geometry and related levels of fusion at millimeter-scale is introduced. An original method to experimentally calibrate the heat input developed to improve the accuracy of the simulations follows. Then, the paper introduces a direct measurement of in-situ molten pool geometries on a single-layer multi-track experiment. To monitor the fast and reduced-size melt pool dimensions, high-speed video recording was used together with a dedicated method to extract the width and length from the images obtained. A comparison between the simulated and the experimentally measured molten pool dimensions follows for validation purposes. Finally, the analysis of the predicted levels of fusion reveal and explain one mechanism of lack of fusion defect appearance and make it possible to demonstrate how the model can be of value in a process parameter optimization procedure.

2. Material and Method

The workflow, illustrated figure 1, follows a standard and consolidated approach in process simulation, which appears to have been neglected in the case of SLM. Previous works of our group have identified the model, applied the heat source calibration and implemented the solver. The

following summarizes these phases, concentrating on the final simulation and validation aspects.

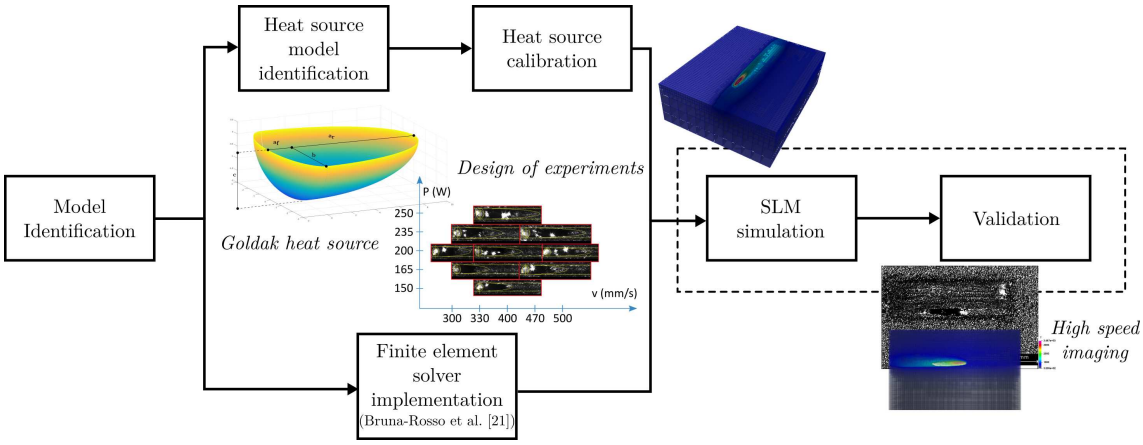

Figure 1: FEM of the SLM process development framework - The dashed rectangle represents the boundary of the work presented here

2.1. Finite Element Model

The model under study is an FEM that was developed in-house and implemented using the deal.ii library [20]. A comprehensive description of the model can be found elsewhere [21] and its main features will be recalled here.

2.1.1. Mathematical Formulation

The current model aims at simulating layer-based selective laser melting of metal at mm-scale. Among the main features that must be considered in the SLM simulation are :

- A moving heat source with a prescribed trajectory
- Convective cooling and radiation between the free surfaces of the part and the building chamber atmosphere
- Description of the phase changes solid $\leftrightarrow$ liquid and powder $\rightarrow$ consolidated material
- Temperature- and phase-dependent material properties

The main simplifying assumptions are the following:

- The melt pool fluid dynamic is not included
- The powder is considered as a homogeneous material

The assumptions are standard considering the geometrical scale modeled (see for example [22]). They were adopted to limit the computational load to tractable levels. The characteristics translate into the following partial differential equation system:

$$\begin{cases} c_p(T)\rho(T)\frac{\partial T(\mathbf{x},t)}{\partial t} - \nabla \cdot k(T)\nabla T(\mathbf{x},t) &= f(\mathbf{x},t) & \text{on } \Omega,\ \text{t} >0 \\ T(\mathbf{x},t) &= T_{\text{amb}} & \text{on } \Omega,\ \text{t} = 0 \\ T(\mathbf{x},t) &= T_{\text{amb}} & \text{on } \Gamma_D,\ \text{t} >0 \\ k(T)\,\frac{\partial T(\mathbf{x},t)}{\partial n} &= \alpha(T) & \text{on } \Gamma_R,\ \text{t} >0 \\ k(T)\,\frac{\partial T(\mathbf{x},t)}{\partial n} &= 0 & \text{on } \Gamma_N,\ \text{t} >0 \end{cases} \tag{1}$$

with :

$\rho = \rho(T, \Phi)$, $c_p = c_p(T, \Phi)$, $k = k(T, \Phi)$, $\alpha(T) = \sigma\varepsilon(T^4 - T_{\text{amb}}^4) + h(T - T_{\text{amb}})$

where :

T is the temperature (K), Φ is the fraction of powder/consolidated (solid or liquid) material, ρ is the density ($\mathrm{kg\,m^{-3}}$), k is the thermal conductivity ($\mathrm{W\,m^{-1}\,K^{-1}}$), c_p is the thermal capacity ($\mathrm{J\,kg^{-1}\,K^{-1}}$), T_{amb} is the ambient temperature in the building chamber (K), h is the convection coefficient ($\mathrm{W\,m^{-2}\,K^{-1}}$), ε is the material emissivity, σ is the Stefan-Boltzmann constant. Ω is the complete domain, Γ_D is the contact area with the substrate where a fixed temperature (Dirichlet) boundary condition (BC) is applied, Γ_R is the contact area with the environing gas which is where radiation and convection cooling occur (Robin BC), and Γ_N are the lateral faces, embedded in the substrate, that were deemed adiabatic (Neumann BC). An illustration of the model with the repartition of the different BC domains can be found in figure 4. $f(\mathbf{x}, t)$ is the heat input provided by the laser (see subsection 2.1.2) and the phase changes (see subsection 2.1.3).

The density ρ is computed according to the experimentally-based model of Mills [23]. It takes into account the temperature, the phase fraction and the powder fraction. The emissivity model, whose full derivation can be found elsewhere [24], accounts for the particle packing, size, and the influence of interstitial spaces. The consolidated material heat conductivity, as well as the heat capacity are computed using [25], while an equivalent homogeneous heat conductivity was implemented for the powder bed following the model of Sih & Barlow [24]. The fully-discrete formulation was derived using the implicit backward-Euler method for time discretization and first order Lagrange finite elements for space discretization. A standard Newton-Raphson algorithm was used for the problem linearization.

2.1.2. Laser Modeling

Two models of laser heat source have been implemented. The first is the phenomenological double ellipsoid model of Goldak [26]. An original method has been developed in-house to compute experimentally calibrated parameters (see subsection 2.1.4. The second model, whose complete description can be found in [18], was implemented in order to derive a model similar to the one of Hodge et al. [19] for numerical validation purposes. The Goldak model was preferred over the Gusarov one in simulations using industrial parameters. In fact, it appeared to better represent the apparent heat density elongation due to the fast laser displacements imposed in industrial SLM process conditions.

Goldak heat source . The power density Q ($\mathrm{W\,m^{-3}}$) of the Goldak heat source is described by the following equations:

$$\begin{aligned} Q &= \frac{6\sqrt{3}P\alpha}{a_f bc\pi\sqrt{\pi}} \exp[-(\frac{3x^2}{a_f^2} + \frac{3y^2}{b^2} + \frac{3z^2}{c^2})] \quad \text{if x>0} \\ Q &= \frac{6\sqrt{3}P\alpha}{a_r bc\pi\sqrt{\pi}} \exp[-(\frac{3x^2}{a_r^2} + \frac{3y^2}{b^2} + \frac{3z^2}{c^2})] \quad \text{if x<0} \end{aligned} \tag{2}$$

Where x, y and z are the coordinates in the referential of the moving laser (i.e. with the origin at the center of the beam) P is the nominal laser power (W) and α is the absorption efficiency. a_r, a_f, b and c are the geometric parameters of the rear and front quadrant, respectively, of the double ellipsoid heat source.

Gusarov heat source . The surface power density Q ($\mathrm{W\,m^{-2}}$) is described by the following equation:

$$\begin{aligned} Q = Q_0\Big[\frac{\rho_h a}{(4\rho_h - 3)D} \times \Big([1-\rho^2]e^{-\lambda}[(1-a)e^{-2a\xi} + (1+a)e^{2a\xi}] - \\ [3+\rho e^{-2\lambda}][(1+a-\rho_h(1-a))e^{2a(\lambda-\xi)} + (1-a-\rho_h(1+a))e^{2a(\xi-\lambda)}]\Big) - \\ \frac{3(1-\rho_h)(e^{-\xi} - \rho_h e^{\xi-2\lambda})}{4\rho_h - 3}\Big] \end{aligned} \tag{3}$$

Where Q_0 is the surface intensity distribution ($\mathrm{W\,m^{-2}}$), given by $Q_0 = \frac{3P}{\pi R^2}(1-\frac{r}{R})^2(a+\frac{r}{R})^2$ where P is the nominal power of the laser (W), R is the laser radius and r is the distance from one point to the laser beam center (m). ρ_h is the hemispherical reflexivity of the powder, $\xi = \beta_h z$ is the dimensionless through-thickness coordinate, β_h is the extinction coefficient , $a = \sqrt{1-\rho_h}$ is a constant, $\lambda = \beta_h L$ is the optical thickness and $D = (1-a)(1-a-\rho_h(1+a))e^{-2a\lambda} - (1+a)(1+a-\rho_h(1-a))e^{2a\lambda}$ is a constant. Finally, the volumetric heat source due to the absorption of laser radiation $q(x,y,z,t)$ ($\mathrm{W\,m^{-3}}$) is given by:

$$q(z,y,z,t) = -\frac{\partial Q}{\partial z} \tag{4}$$

2.1.3. Phase Change

During the SLM process, two major types of phase change, irreversible and reversible occur:

- irreversible: powder $\longrightarrow$ consolidated (liquid or solid)
- reversible: solid $\longleftrightarrow$ liquid

A fictitious heat source method, introduced by Rolph & Bathe [27] was adapted and used to model both phase changes. This algorithm consists in computing a heat source equivalent to the amount of latent heat either absorbed or released during one time step at each node undergoing phase changes, until complete melting or solidification. It permits tracking of the fraction of powder at each node, which renders possible the detection of lack of fusion due to an insufficient heat input.

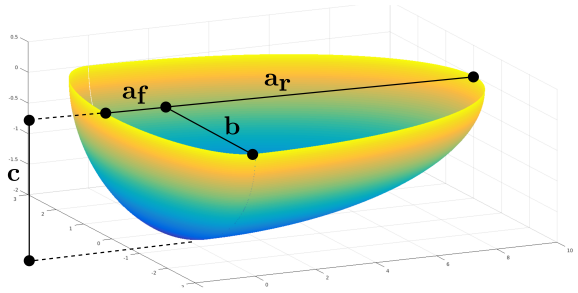

Figure 2: Goldak heat source geometry and parameters

2.1.4. Goldak heat source calibration

The parameters present in the Goldak heat source formulation of equation 2 are measured from the melt pool geometry in single-track welding experiments [26]. They are illustrated in figure 2. They thus depend on the material and process parameters. As the laser power and speed are two of the most influential parameters of the laser manufacturing processes, it is necessary to modify the Goldak parameters to be used in the FEM according to them. Empirical models $f(P, v) \rightarrow b$ and $f(P, v) \rightarrow c$ were therefore obtained using design of experiment techniques. For this purpose a central composite design (CCD) of experiment with two parameters (P and v) was performed. The hardware that was used for the calibration procedure is the same as the one presented section 2.2.1. As suggested by the authors of the original model , a_f and a_r may be determined as a function of the melt pool half-width b using the following relationships: $a_r = 4 \times b$ and $a_f = b$. However, preliminary observations of the melt pool geometries showed that those relationships do not apply when using process parameters optimized for the SLM of AISI316L stainless steel. That is why new proportionality factors, k_r and k_f, will be determined using in-process images recorded by a high-speed video camera: $a_r = k_r \times b$ and $a_f = k_f \times b$.

The levels chosen for each parameter in the CCD and the corresponding melt pool geometries obtained are displayed in figure 3.

$$2 \times b = 144.3 + 0.814 \times P - 0.358 \times v + 0.000509 \times v^2 - 0.000967 \times P \times v \tag{5}$$

$$c = 41.9 + 0.1768 \times P - 0.06425 \times v \tag{6}$$

$$k_r = 8.8 \tag{7}$$

$$k_f = 0.8 \tag{8}$$

The empirical models and the new proportionality coefficients that were derived are displayed in equations 5 - 8.

The corresponding values of the Goldak parameters obtained for the process parameters used in the present study are recalled in table 1.

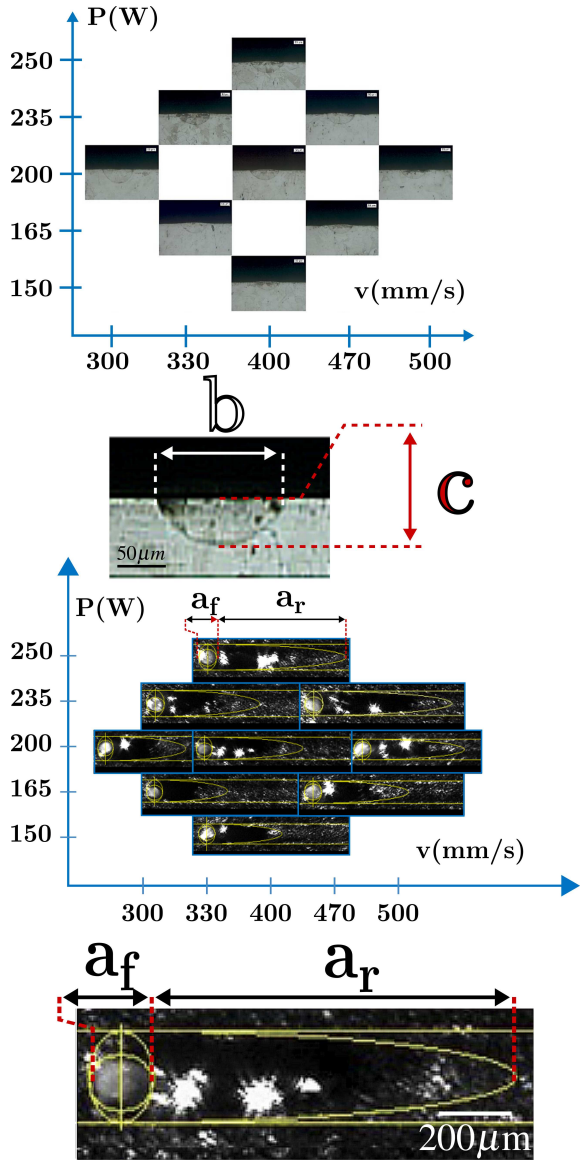

Figure 3: Welding CCD and corresponding melt pool geometries

Table 1: Experimentally calibrated Goldak parameters

a_f	a_r	b	c
67×10^{-6} m	757×10^{-6} m	84×10^{-6} m	58×10^{-6} m

2.1.5. Model validation

A simulation reproducing the experiment described in section 2.2.1 was performed to experimentally validate the model. The model at the beginning of the simulation is illustrated in figure 4.

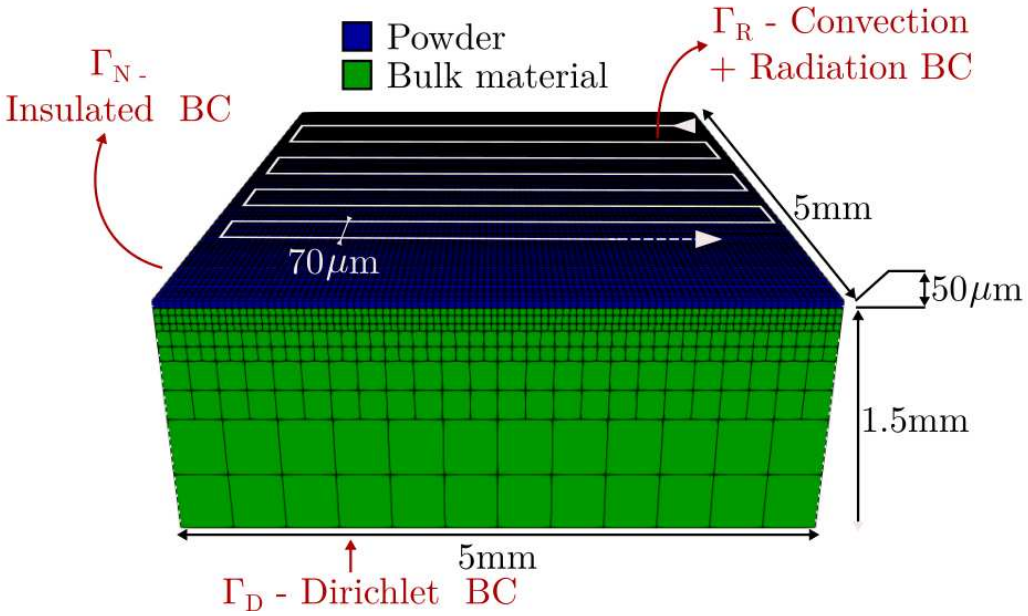

Figure 4: FEM corresponding to the HSI experiment

Figure 4 shows that the mesh features hexahedral elements of various sizes, which vary from 20 to 300 µm. Adaptive mesh refinement was implemented to ensure the presence of elements that were fine enough where needed (i.e. in the powder layer and where the thermal gradients are the highest) and a coarser mesh elsewhere to limit the computational load of the model.

2.2. High-speed imaging

2.2.1. Experimental setup

An SLM experiment was performed on the AISI316L stainless steel. The machine used was an SLM prototype [28] that was built in-house. The laser source and the optical chain reproduce the one of the industrial system RENISHAW AM 250. The utilization of this hardware makes it possible to perform reduced-size tests and provides high flexibility for the installation of various devices for monitoring purposes [29]. In the current study, the experiment was recorded using a FASTCAM Mini AX200 high-speed video camera synchronized with a CAVILUX HF laser illuminator. An optical bandpass filter at 640+/-10 nm was placed in front of the high-speed camera to suppress the process emission. A photograph and a scheme of the experimental setup are displayed in figure 5. The recording speed was set to 50000 frames per second. One layer of 3x3 mm^2 was processed using a 70 µm hatching distance which corresponds to 42 tracks. The gas atomized AISI 316L stainless steel powder used had the following characteristics: the apparent density was 4.07 $g\,cm^{-3}$

Table 2: Parameters of high-speed imaging monitored experiment

Parameter	Value
Laser power	250W
Laser speed	500mm/s
Laser diameter	60µm
Material	AISI316L Stainless steel
Hatching distance	70µm
Layer thickness	50µm
Scan strategy	Meander

whilst the powder size distribution was D10: 23 µm, D50: 32 µm, D90: 44 µm. The characteristics of the experiments are regrouped in table 2. The process parameters correspond to industrial working conditions.

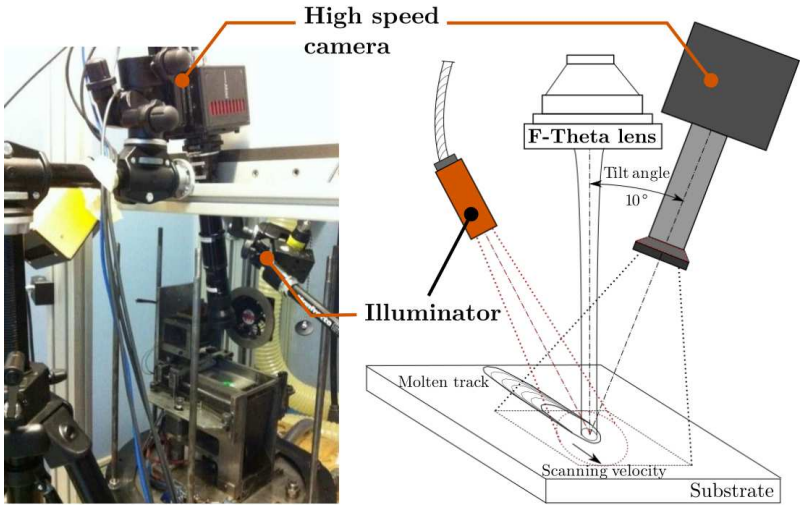

Figure 5: HSI experimental setup

2.2.2. Melt pool measurements

Prior to image acquisitions, the size of the imaging field was measured using a calibrated artifact. The procedure used to measure the melt pool length and width on images taken from the high-speed video utilizes two properties: the laser irradiated area, which is the brightest region, and the liquid metal, which is darker than its environment. It is thus possible to discriminate the pixels that belong to the laser spot (resp. melt pool) using their levels of grey:

- Pixels having a grey level of 255 are part of the laser irradiated zone
- Pixels having a grey level of 0 are part of the melt pool

This method, which can be applied using image processing software, consists in the following steps illustrated in figure 6.

1. Contrast increase and sharpening
2. Extraction of the grey level along two lines corresponding to cross sections on the xz and yz planes
3. Conversion of pixel measurements into dimensions using the previously determined calibration factor

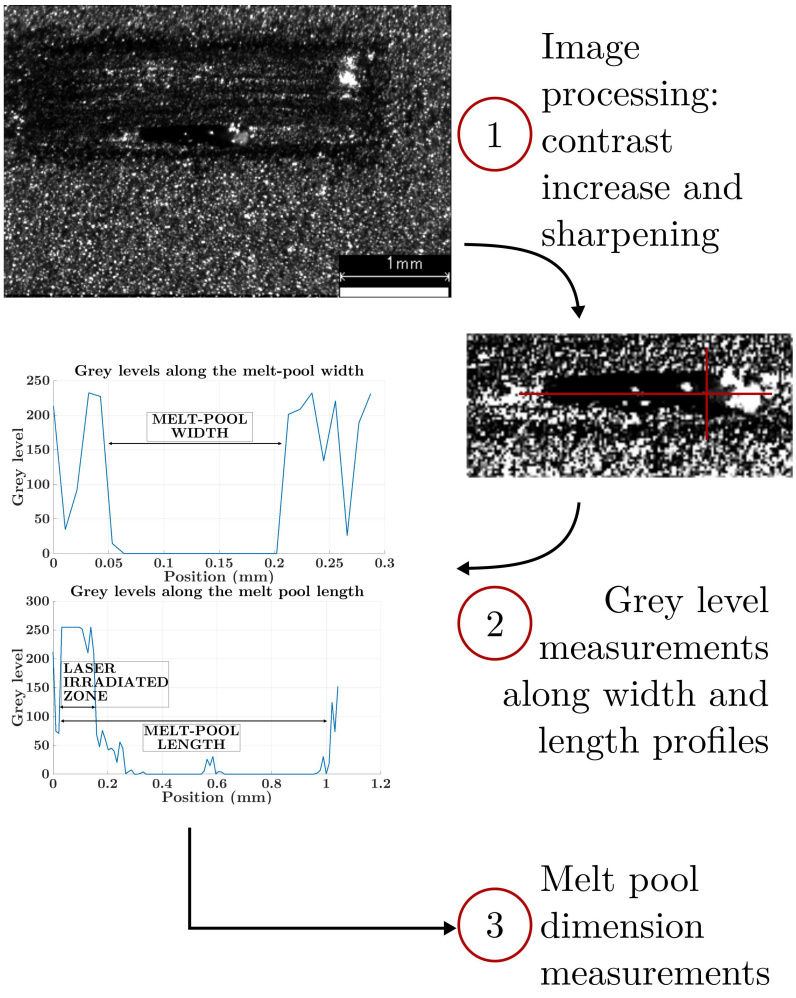

Figure 6: Melt pool measurement from the HSI method

Melt pool measurements for each track from the third to the twenty-second one were taken near the middle of the tracks. For the experimental measurements on the high-speed video three measures per track were performed, from which the means and standard deviations were retrieved. Within a single track the images extracted from the video for melt pool measurements are separated by 5 frames. Considering the recording speed (50000 fps) and the laser velocity (500 mm/s), the total length between the two extreme frames is 50µm, which is lower than the diameter of the laser (60µm). The simulated melt pool geometries were steady enough around the positions considered for a single sizing to be deemed sufficient. The other tracks were not showing enough contrast to clearly identify the melt pool and were thus not considered.

Table 3: Numerical validation simulation parameters (adapted from [15] and [16])

Parameter	**Value**
Geometry	0.6x0.2x0.2 mm^3
Effective laser power	30 W
Laser speed	120 mm/s
Hemispherical reflexivity	0.7
Laser beam radius	60 µm

3. Results

3.1. Numerical Validation

As a first validation step, the present model was compared to results retrieved from the literature [18, 19]. A single-track reduced-scale simulation reproducing the one reported in both articles was run. The main parameters of this simulation are recalled in table 3. The heat input travels from x = 0 to x = 0.5 mm at the center of the block on the y axis. The surfaces are all given a Neumann boundary condition except for the one at x = 0.6 mm to which a Dirichlet BC ($T = 303$K) was assigned. The results obtained are reported in figure 7 and table 4.

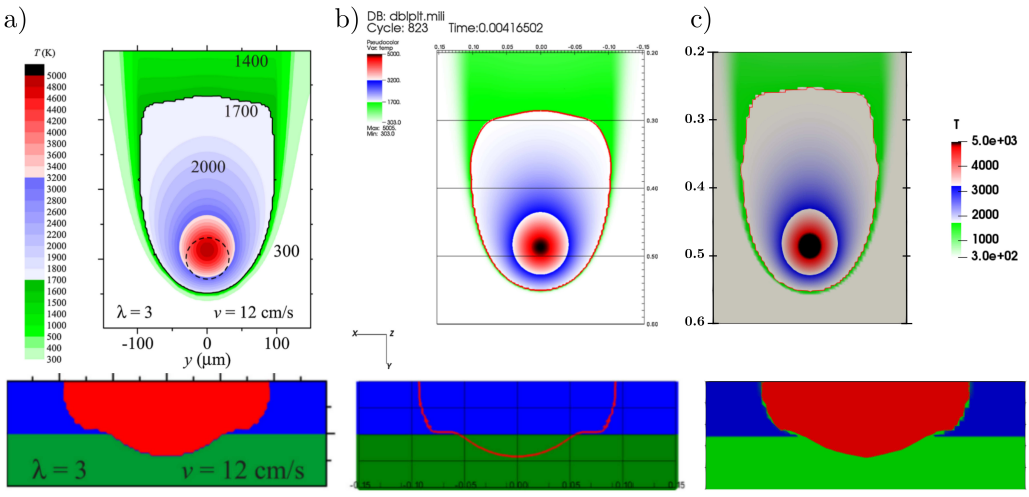

Figure 7: Numerical validation results. Top : xy plane view of the melt pool and thermal field. Bottom: xz view of the phase distribution (blue: solid - green: powder - red: liquid)

a) Results from Gusarov et al. [15]

b) Results from Hodge et al. [16]

c) Our results

We observed that in terms of melt pool geometry, the results are very close to the ones obtained by Gusarov [18] while being slightly higher than those reported by Hodge [19]. The maximal temperature is higher than the one obtained by the two other models, but still remains within a 10% relative difference. The discrepancies can be explained by slight differences in the phase change model implementation which could not take into account the exact same material properties

Table 4: Numerical validation results - Maximal temperatures and melt pool dimensions

	Gusarov	**Hodge**	**Our results**
T_{max} (K)	4900	5000	5400
Melt pool length (mm)	0.300	0.263	0.308
Melt pool width (mm)	0.200	0.208	0.209
Melt pool depth (mm)	0.070	0.065	0.071

evolution during the powder to solid transformation. Nevertheless the accordance between the results of the present model and those from the literature was deemed sufficient to numerically validate it.

3.2. Validation with the high-speed videos

Measurements of the melt pool using the method described section 2.2.2 were compared to the geometries obtained from a simulation reproducing the experimental conditions in which the video was recorded. A typical example, taken in the middle of the ninth track, of melt pool geometry obtained from the experiment and the corresponding simulation is shown in figure 8. The measurements from track 3 to 32 are displayed in figure 9. The experimental measurement points correspond to the means of the three measurements while the error bars correspond to their standard deviations.

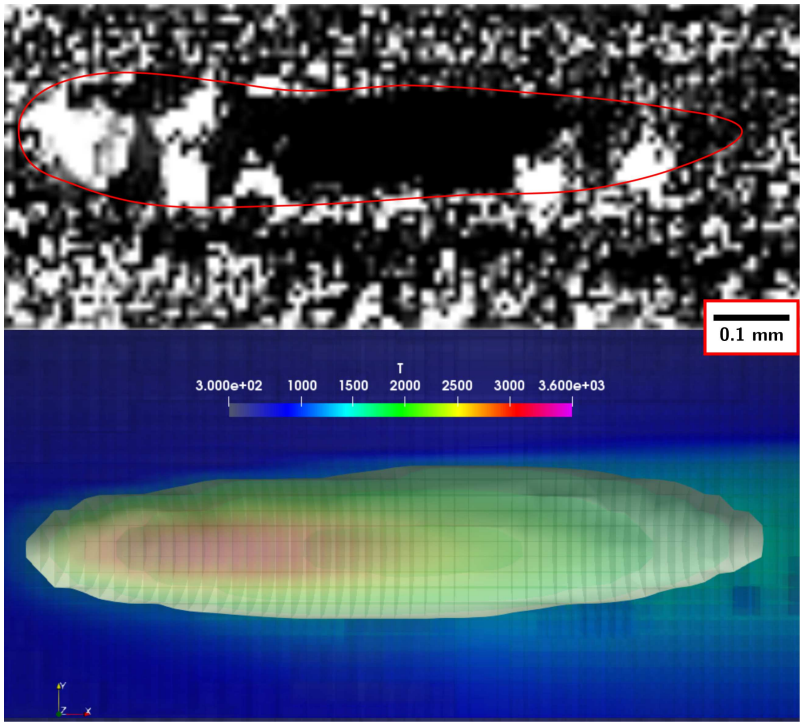

Figure 8: Experimental and corresponding simulated melt pool

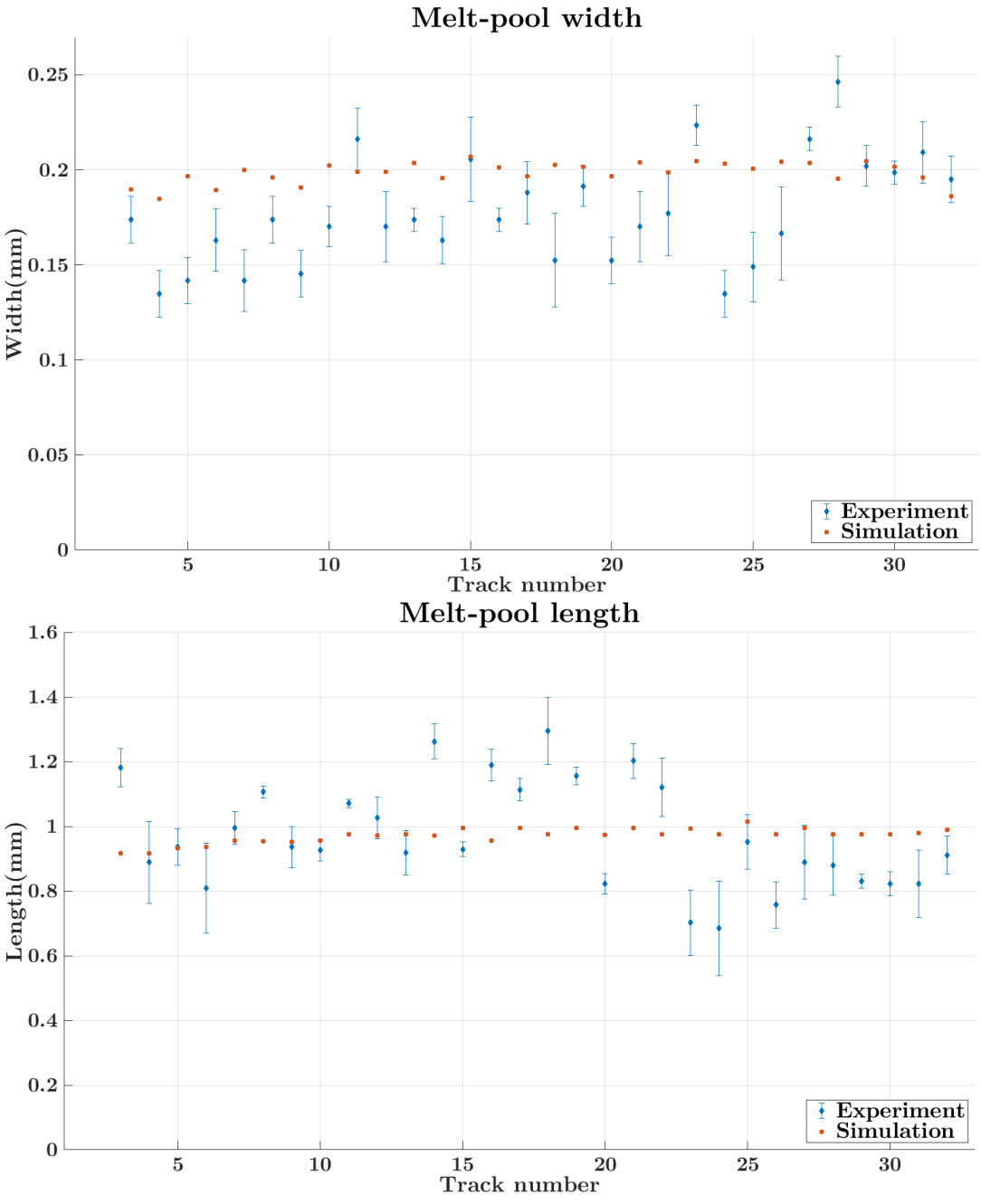

Figure 9: Experimental vs. simulated melt pool width and length

Figure 9 shows that the model is able to fairly accurately replicate the melt pool geometry that was experimentally measured. One of the main goals of the present study, namely computing melt pool geometries in a millimeter-scale and multi-track experiment representative of the real ones, is thus fulfilled. The discrepancies nonetheless observed may be explained by the simplifying assumption on which the present model is based. First, the model does not include the melt pool fluid dynamics, previously mentioned as being influential on the melt pool dimensions and temperatures (see [30, 31] for example). Various phenomena occurring in the molten metal could not be represented: capillary forces (surface tension), Marangoni convection, recoil pressure, buoyancy and drag forces due to the solid/liquid transition. They generate phenomena that are known to produce balling effects and subsequent porosity (see [32] for example). Second, homogenization of the powder bed prevents the modeling of the effect of powder unevenness on the process. As a consequence, phenomena related to the discrete nature of the powder such as denudation and spatter [33] cannot be modeled. They have been demonstrated to have a significant effect on the surface roughness and porosity formation [34]. Finally, there is no gaseous phase inside the model. The absence of vaporization prevents the simulation of the key-hole effect that was identified as a significant source of porosity generation in SLM-produced parts [35]. The gas flow effects are only represented through the convection BC on the top surface, and their mechanical action on the melt pool is not represented. All phenomena mentioned previously have an influence on the temperature field, and as a consequence on the melt pool geometry. Most of them are cooling phenomena, and would thus produce lower computed temperatures, not exceeding the vapor point of the material under study. Using identical heat inputs, models including all the cited phenomena would produce smaller melt pool dimensions (with the exception of process conditions leading to keyhole effects) with respect to finite element models such as the present one. However, the utilization of the empirical model presented section 2.1.2 coupled with the experimental calibration presented in section 2.1.4 was deemed to partially include their effects and thus participate in reducing this discrepancy. Since the Goldak heat source was calibrated on welding experiments, the powder effects are not represented but the molten metal dynamics and gaseous effects can be caught.

The simplifying assumptions adopted also explain the steadiness of the geometry predicted by our model while significant variabilities are observed in the experimental melt pool measurements. Indeed, it does not include the phenomena responsible for the melt pool instabilities.

However addition of a mass transport term in equation 1 would bring significant complexity to the model, and studies including those phenomena are limited to reduced domain [6]. Discretization of the powder further increases the complexity and consequently the computational load of the simulations. All the previously-cited study were limited to a few hundred micrometers in single-track simulations. The lack of fusion defects, or the evolution of the melt pool geometry between tracks cannot be shown in such simulations while finite elements efficiency allows the utilization of bigger domains. New methods are being developed to improve the FEM representativity. Ladani

et al. [36] recently proposed to introduce an equivalent heat conduction coefficient including the melt pool fluid dynamic thermal effects. That makes it possible to take into account buoyancy and Marangoni effects at an affordable computational cost. Subsequent studies may implement this technique and assess its influence on the predictive capacities of the model.

These simplifications limit the study of the influence that a parameter has on the process quality to that of the power density, i.e. whether the heat input and how it spreads inside the part allows melting of the requested amount of powder. However, recent works demonstrated that it is not sufficient to assess the suitability of one set of process parameters [37]. Nevertheless, the correlation model/experiment remains satisfying and ensures that despite the simplifying choices that were made, the main thermal phenomena are caught by the finite element model.

3.3. Lack of fusion defect prediction

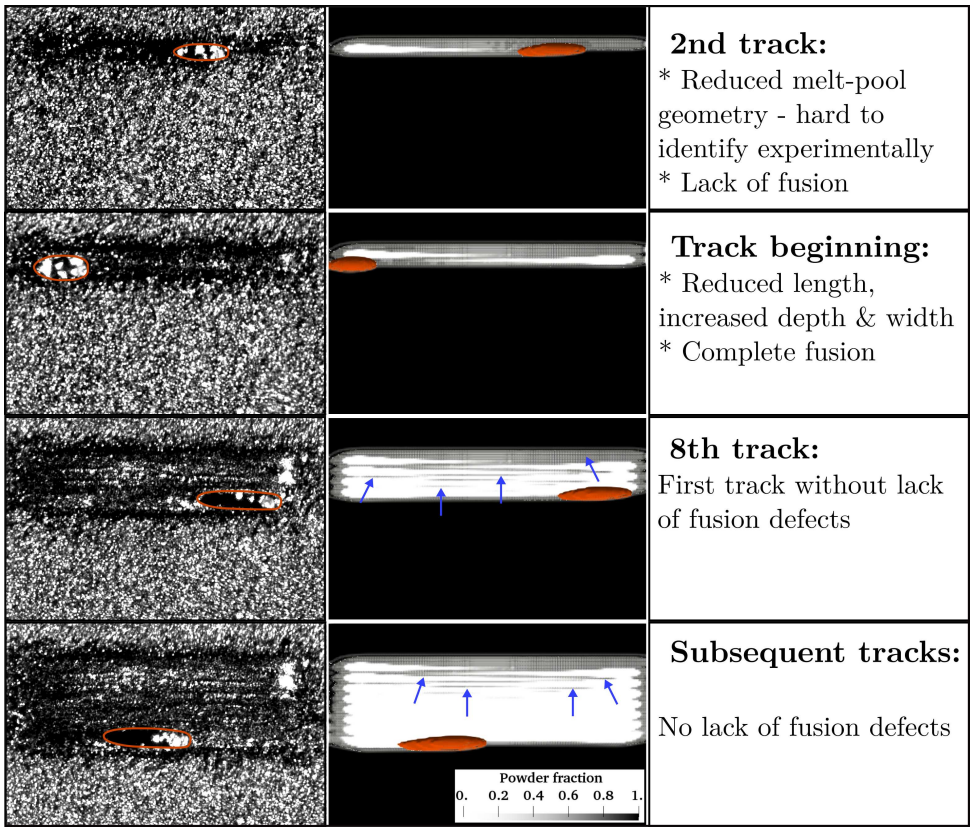

Figure 10: Melt pool evolution in four building steps. Blue arrows indicate lack of fusion defects. Orange contours approximately delimit the experimental molten pools.

As introduced in section 2.1.3, the model includes a phase change algorithm that was used to track the level of fusion at each node of the FE mesh. With this tool it is possible to model the lack of fusion defects that may appear when the heat input in a certain area is not sufficient and powder grains remain un-melted. In the results of the simulation described in section 2.1.5, such defects are observable in the first tracks as illustrated in figure 10. This highlights a lack of thermal energy in

those points, which leads to a reduced melt pool size. The smaller dimensions lead to lacks of fusion in the first tracks. After the 8th track, there is no more unfused powder due to insufficient heating. It appeared in the simulation that the process needs a few tracks to "settle" and stabilized itself in a rather constant melt pool geometry. This phenomenon was previously predicted by Foroozmehr et al. [12], which showed that when comparing the melt pool dimensions at the same position on the X-axis, they are smaller on the first tracks with respect to the subsequent ones. This may be due to the fact that the equilibrium between the heat source (i.e. the laser energy) and the heat sink (mostly, the consolidated material) is not immediate. It requires a certain amount of melted/consolidated material around the melt pool to create an efficient thermal bond with the substrate, since the powder has a much lower heat conductivity than the bulk material. Efficient conduction allows the thermal energy provided by the laser to spread evenly around the heat affected zone. The powder tends to restrain it, so producing the reduced melt pool geometries observed. Several tracks are needed to fully break the thermally insulating barrier created by the powder bed. Increased heat density would thus be needed to ensure full melting in the first tracks. This is further highlighted by the reduction of this phenomenon at the extremities of the tracks where the concentration of heat is higher due to the meander trajectory. However, one has to remember not to overcome the thermal energy input threshold that would create too many vaporization and produce the so-called "keyhole effect" which would generate porosity as well [35]. This effect would not appear in the present simulation since the liquid-vapor phase change is not modeled. The model reproduced one of the mechanisms that produces porosity defects, or so-called "acicular" (i.e. elongated) pores [38]. It can be of value to predict their occurrence by studying the potential effects of process parameters, and determine a working window where they do not appear, or at least are undermined. The model may thus be used to diminish the process-induced defects. Improving the understanding of this mechanism of lack of fusion defect formation in SLM is in fact still an open issue [39]. The simulation results suggest that a different set of process parameters should be used in the first tracks in order to reach full melting, which is not currently possible to implement in most industrial SLM hardware. The model can be used to perform reduced scale computational experiments to derive correction tables to adapt either the scanning strategy or the process parameters in the first tracks, so preventing this phenomenon during the manufacturing strategy design. Indeed, the current computational efficiency of the model does not allow the running of full-scale simulation and optimization of the process parameters numerically. However, coupled with an experimental approach, it is worthwhile to understand the defect formation mechanisms due to varying thermal energy distributions generated by different parameters (geometry, track length, track number etc.). This may be of use to orientate the process optimization procedure, and thus speed it up.

4. Conclusion

An in-house SLM finite element model was developed to compute the thermal field at mm-scale and the consequent melt pool geometry and temperature. As a result, the level of fusion during multi-track SLM was disclosed and lack of fusion-related porosities were predicted. The in-house FEM that was implemented was preliminarily validated numerically by reproducing simulation results from the literature. Then, in order to verify simulation output, an experimental apparatus was conceived to allow for high-speed video recording of the process on the multi-track field of view. Thanks to the high spatial and temporal resolution of the high-speed camera and to the contribution of a synchronized illuminator, the molten pool geometry was detected in line during the SLM of AISI316L stainless steel in representative industrial conditions. The experimental data retrieved was used for not only basic understanding of the SLM but also to produce results for validation purposes. Each step of the model development, from its implementation, to the validation stage through experimental calibration of the heat input were performed in-house. This provides two open platforms, one hardware and the other software, which enable the prediction and sensing of direct attributes of the melt pool that affect SLM process quality. The main conclusions that can be drawn from the obtained results are the following:

- Quantitative data on the melt pool geometries are available after extraction and dedicated post-processing from a high-speed video of a single layer multi-track SLM experiment;
- Computed data on the melt pool geometries are provided by a simplified FEM model reproducing thermal phenomena during SLM of a single layer multi-track;
- The computed melt pool dimensions are in fair agreement with those measured from the high-speed videos, considering the simplifying assumptions on which the FEM was developed (no melt pool fluid-dynamics and homogenized powder bed)
- The powder fraction-field revealed lack of fusion in the first tracks arising from insufficient heat conduction due to an excessive quantity of powder around the melt pool, which has an insulating effect.
- The model highlights the potential advantages of in-building adaptive process parameters and
- is relevant used together with experiments to give directions on how to modify them and thus speed up the procedure of parameter optimization.

Further work involving the computational design of experiment can be used to derive empirical models to link to process parameter modifications with respect to their nominal values. Having such a tool at hand would be of use to orientate the parameter optimization procedure without running additional lengthy SLM experiments and thus reduce the time and costs of the process design stage through the definition of a-priori knowledge provided by simulation.

Acknowledgements

The authors gratefully acknowledge the technical support and collaboration of BLM Group, IPG Photonics Italy, and Renishaw. This work was supported by Regione Lombardia in the frame of the project MADE4LO under the call "POR FESR 2014-2020 ASSE I - AZIONE I.1.B.1.3 and by the autonomous province of Trento (Italy), through Regional Law 6/98 (Project: LT4.0).

Data availability statement

The raw and processed data required to reproduce these findings are available upon request to the corresponding author.

References

[1] D. D. Gu, W. Meiners, K. Wissenbach, R. Poprawe, Laser additive manufacturing of metallic components: materials, processes and mechanisms, International Materials Reviews 57 (3) (2012) 133–164. doi:10.1179/1743280411y.0000000014.

[2] C. Y. Yap, C. K. Chua, Z. L. Dong, Z. H. Liu, D. Q. Zhang, L. E. Loh, S. L. Sing, Review of selective laser melting: Materials and applications, Applied Physics Reviews 2 (4). doi:10.1063/1.4935926.

[3] W. E. Frazier, Metal additive manufacturing: A review, Journal of Materials Engineering and Performance 23 (6) (2014) 1917–1928. doi:10.1007/s11665-014-0958-z.

[4] A. G. Demir, B. Previtali, Investigation of remelting and preheating in SLM of 18Ni300 maraging steel as corrective and preventive measures for porosity reduction, The International Journal of Advanced Manufacturing Technologydoi:10.1007/s00170-017-0697-z.

[5] H. Bikas, P. Stavropoulos, G. Chryssolouris, Additive manufacturing methods and modelling approaches: a critical review, The International Journal of Advanced Manufacturing Technology 83 (1) (2016) 389–405. doi:10.1007/s00170-015-7576-2.

[6] M. Markl, C. Körner, Multiscale modeling of powder bed-based additive manufacturing, Annual Review of Materials Research 46 (1) (2016) 93–123. doi:10.1146/annurev-matsci-070115-032158.

[7] B. Schoinochoritis, D. Chantzis, K. Salonitis, Simulation of metallic powder bed additive manufacturing processes with the finite element method: A critical review, Proceedings of the Institution of Mechanical Engineers, Part B: Journal of Engineering Manufacturedoi:10.1177/0954405414567522.

[8] Y. Huang and L.J. Yang and X.Z. Du and Y.P. Yang, Finite element analysis of thermal behavior of metal powder during selective laser melting, International Journal of Thermal Sciences 104 (2016) 146 – 157. doi:http://dx.doi.org/10.1016/j.ijthermalsci.2016.01.007.

[9] S. Roy, M. Juha, M. S. Shephard, A. M. Maniatty, Heat transfer model and finite element formulation for simulation of selective laser melting, Computational Mechanicsdoi:10.1007/s00466-017-1496-y.

[10] D. Pitassi, M. Benedetti, E. Savoia, V. Fontanari, A. Molinari, V. Luchin, G. Zappini, Finite element thermal analysis of metal parts additively manufactured via selective laser melting, in: P. Rzvan (Ed.), Finite Element Method, InTech, Rijeka, 2018, Ch. 6. doi:10.5772/intechopen.71876.

[11] K. Antony, N. Arivazhagan, K. Senthilkumaran, Numerical and experimental investigations on laser melting of stainless steel 316L metal powders, Journal of Manufacturing Processes 16 (3) (2014) 345–355. doi:10.1016/j.jmapro.2014.04.001.

[12] A. Foroozmehr, M. Badrossamay, E. Foroozmehr, S. Golabi, Finite element simulation of selective laser melting process considering optical penetration depth of laser in powder bed, Materials & Design 89 (2016) 255 – 263. doi:10.1016/j.matdes.2015.10.002.

[13] R. Andreotta, L. Ladani, W. Brindley, Finite element simulation of laser additive melting and solidification of inconel 718 with experimentally tested thermal properties, Finite Elements in Analysis and Design 135 (Supplement C) (2017) 36 – 43. doi:10.1016/j.finel.2017.07.002.

[14] E. R. Denlinger, V. Jagdale, G. Srinivasan, T. El-Wardany, P. Michaleris, Thermal modeling of inconel 718 processed with powder bed fusion and experimental validation using in situ measurements, Additive Manufacturing 11 (2016) 7 – 15. doi:10.1016/j.addma.2016.03.003.

[15] B. Cheng, S. Price, J. Lydon, K. Cooper, K. Chou, On process temperature in powder-bed electron beam additive manufacturing: Model development and validation, Journal of Manufacturing Science and Engineering 136 (6) (2014) 061018.

[16] D. Riedlbauer, T. Scharowsky, R. F. Singer, P. Steinmann, C. Körner, J. Mergheim, Macroscopic simulation and experimental measurement of melt pool characteristics in selective electron beam melting of Ti-6Al-4V, The International Journal of Advanced Manufacturing Technology 88 (5) (2017) 1309–1317. doi:10.1007/s00170-016-8819-6.

[17] U. Scipioni-Bertoli, G. Guss, S. Wu, M. J. Matthews, J. M. Schoenung, In-situ characterization of laser-powder interaction and cooling rates through high-speed imaging of powder bed fusion additive manufacturing, Materials & Design 135 (2017) 385 – 396. doi:10.1016/j.matdes.2017.09.044.

[18] A. Gusarov, I. Yadroitsev, P. Bertrand, I. Smurov, Model of radiation and heat transfer in laser-powder interaction zone at selective laser melting, J. Heat Transfer 131 (7) (2009) 072101.

[19] N. E. Hodge, R. M. Ferencz, J. M. Solberg, Implementation of a thermomechanical model for the simulation of selective laser melting, Computational Mechanics 54 (1) (2014) 33–51. doi:10.1007/s00466-014-1024-2.

[20] D. Arndt, W. Bangerth, D. Davydov, T. Heister, L. Heltai, M. Kronbichler, M. Maier, J.-P. Pelteret, B. Turcksin, D. Wells, The deal.II library, version 8.5, Journal of Numerical Mathematics 25 (3) (2017) 137–146. doi:10.1515/jnma-2016-1045.

[21] C. Bruna-Rosso, A. G. Demir, B. Previtali, M. Vedani, Selective laser melting high performance modeling, in: I. Drstvenek, D. Drummer, M. Schmidt (Eds.), Proceedings of 6th International Conference on Additive Technologies, Interesansa - zavod, Ljubljana, 2016, pp. 252 – 259.

[22] W. E. King, A. T. Anderson, R. M. Ferencz, N. E. Hodge, C. Kamath, S. A. Khairallah, A. M. Rubenchik, Laser powder bed fusion additive manufacturing of metals; physics, computational, and materials challenges, Applied Physics Reviews 2 (4). doi:10.1063/1.4937809.

[23] K. C. Mills, Fe - 316 stainless steel, in: K. C. Mills (Ed.), Recommended Values of Thermophysical Properties for Selected Commercial Alloys, Woodhead Publishing Series in Metals and Surface Engineering, Woodhead Publishing, 2002, pp. 135 – 142. doi:10.1533/9781845690144.135.

[24] S. S. Sih, J. W. Barlow, The prediction of the emissivity and thermal conductivity of powder beds, Particulate Science and Technology 22 (4) (2004) 427–440. doi:10.1080/02726350490501682.

[25] J. K. Panayiotis, B. Marc-Jean, Thermal and structural properties of fusion related materials, http://www-ferp.ucsd.edu/LIB/PROPS/PANOS/ (1997).

[26] J. Goldak, A. Chakravarti, M. Bibby, A new finite element model for welding heat sources, Metall. Trans. B 15 (2) (1984) 299–305. doi:10.1007/BF02667333.

[27] W. D. Rolph, K.-J. Bathe, An efficient algorithm for analysis of nonlinear heat transfer with phase changes, Int. J. Numer. Methods Eng. 18 (1) (1982) 119–134. doi:10.1002/nme.1620180111.

[28] A. G. Demir, L. Monguzzi, B. Previtali, Selective laser melting of pure zn with high density for biodegradable implant manufacturing, Additive Manufacturing 15 (2017) 20 – 28. doi:10.1016/j.addma.2017.03.004.

[29] A. G. Demir, C. De Giorgi, B. Previtali, Design and implementation of a multisensor coaxial monitoring system with correction strategies for selective laser melting of a maraging steel, Journal of Manufacturing Science and Engineering 140 (4) (2018) 041003.

[30] A. Hussein, L. Hao, C. Z. Yan, R. Everson, Finite element simulation of the temperature and stress fields in single layers built without-support in selective laser melting, Materials & Design 52 (2013) 638–647. doi:10.1016/j.matdes.2013.05.070.

[31] A. Bauereiss, T. Scharowsky, C. Körner, Defect generation and propagation mechanism during additive manufacturing by selective beam melting, Journal of Materials Processing Technology 214 (11) (2014) 2522 – 2528. doi:10.1016/j.jmatprotec.2014.05.002.

[32] D. H. Dai, D. D. Gu, Thermal behavior and densification mechanism during selective laser melting of copper matrix composites: Simulation and experiments, Materials & Design 55 (2014) 482–491. doi:10.1016/j.matdes.2013.10.006.

[33] S. A. Khairallah, A. T. Anderson, A. Rubenchik, W. E. King, Laser powder-bed fusion additive manufacturing: Physics of complex melt flow and formation mechanisms of pores, spatter, and denudation zones, Acta Materialia 108 (2016) 36 – 45. doi:10.1016/j.actamat.2016.02.014.

[34] C. Qiu, C. Panwisawas, M. Ward, H. C. Basoalto, J. W. Brooks, M. M. Attallah, On the role of melt flow into the surface structure and porosity development during selective laser melting, Acta Materialia 96 (2015) 72 – 79. doi:10.1016/j.actamat.2015.06.004.

[35] W. E. King, H. D. Barth, V. M. Castillo, G. F. Gallegos, J. W. Gibbs, D. E. Hahn, C. Kamath, A. M. Rubenchik, Observation of keyhole-mode laser melting in laser powder-bed fusion additive manufacturing, Journal of Materials Processing Technology 214 (12) (2014) 2915 – 2925. doi:10.1016/j.jmatprotec.2014.06.005.

[36] L. Ladani, J. Romano, W. Brindley, S. Burlatsky, Effective liquid conductivity for improved simulation of thermal transport in laser beam melting powder bed technology, Additive Manufacturing 14 (Supplement C) (2017) 13 – 23. doi:10.1016/j.addma.2016.12.004.

[37] U. S. Bertoli, A. J. Wolfer, M. J. Matthews, J.-P. R. Delplanque, J. M. Schoenung, On the limitations of volumetric energy density as a design parameter for selective laser melting, Materials & Design 113 (2017) 331 – 340. doi:10.1016/j.matdes.2016.10.037.

[38] M. Grasso, B. M. Colosimo, Process defects and in situ monitoring methods in metal powder bed fusion: a review, Measurement Science and Technology 28 (4) (2017) 044005.

[39] K. Darvish, Z. Chen, T. Pasang, Reducing lack of fusion during selective laser melting of CoCrMo alloy: Effect of laser power on geometrical features of tracks, Materials & Design 112 (2016) 357 – 366. doi:10.1016/j.matdes.2016.09.086.